Scripta Materialia 157 (2018) 157–161

Contents lists available at ScienceDirect

Scripta Materialia

journal homepage: www.elsevier.com/locate/scriptamat

Regular article

Nanocompression of secondary particles of silica aerogel

William Gonçalves[a,b,*], Jonathan Amodeo[a], Julien Morthomas[a], Patrice Chantrenne[a], Michel Perez[a], Geneviève Foray[a], Christophe L. Martin[b]

[a] Université de Lyon, INSA-Lyon, UCBL, CNRS, MATEIS, 7, Avenue Jean Capelle, Villeurbanne cedex 69621, France
[b] Univ. Grenoble Alpes, CNRS, SIMAP, Grenoble F-38000, France

ARTICLE INFO

Article history:
Received 14 June 2018
Received in revised form 26 July 2018
Accepted 29 July 2018
Available online 1 September 2018

Keywords:
Molecular dynamics
Silica aerogel
Multi-scale model
Nanocompression

ABSTRACT

The compression of highly porous silica nanospheres is investigated using molecular dynamics simulations and modeling. The ligaments network (3–6 nm) of nano-sized silica sustains the load and nanoparticles deform plastically due to highly localized shear events, at the junctions between ligaments. Dangling ligaments are more numerous as the size of the nanosphere decreases, thus impacting the mechanical response. Based on simulation results, we propose a scaling law that describes the particle size effect on the indentation force when applied to silica aerogel secondary nanoparticles under compression.

Amorphous silica aerogels are nanoporous materials architectured over several length scales. At the nanoscale, they form a three-dimensional porous network of primary dense particles. Depending on the processing conditions, the primary particle size may vary between 3 and 7 nm [1] while the pore size in the network of primary particles is typically of the order of 10 nm [1-3]. At a larger scale, the porous network of primary particles forms aggregates, defined as secondary particles that might be referred as interconnected silica clusters, and are approximately spherical in shape. The size of secondary particles ranges between 50 and 100 nm [1]. Secondary porous particles arrange at the mesoscale into a granular-like medium [4] with corresponding mesopores of about 50 to 100 nm size. This porous multi-scale architecture originates from the sol-gel reaction and supercritical drying that both lead to the exceptional thermal insulation properties of aerogel-based materials [5]. In contrast to more standard porous insulators, the nanopores of aerogels are interconnected. The highly porous structure of secondary particles (typically for a 250 kg· m^{-3} density, a secondary particle is 90% porous) is obviously beneficial for insulation but at the price of poor mechanical properties.

Aerogel elastic properties may be approached experimentally [6-8] and it is shown that the density dependency of the elastic modulus follows a power law with an exponent of 3.5–3.8, which is typical of fractal structures [8]. Molecular dynamics (MD) simulations are also a powerful tool to investigate these properties. However, past simulations focusing on porous SiO_2 were only carried at the length-scale of a few tenths of nanometers [9-11], with too small pore sizes when compared to the 10 nm range observed in experiments. These simulations offer interesting insights in the inner structure and the mechanical properties of secondary particles but cannot fully reproduce their peculiar heterogeneous microstructure. Also, they cannot model a whole secondary particle and can even less predict their interactions with neighboring secondary particles.

Recently, the use of a van Beest, Kramer and van Santen (BKS) pair potential optimized for larger timescale simulations (without long-range interactions) and transferable to surface properties [12], opened the possibility to explore nanoporous structures with surface/volume ratio that are very close to experimental silica aerogels [13]. Large volumes (up to 100^3 nm^3) were modeled with pores that match satisfactorily experimental observations [1]. The elasticity and strength of these volumes have shown a marked asymmetry in tension-compression that originates from the substantial preexisting compressive capillary-driven stress that silica ligaments are subjected to [13].

Real silica aerogels involve porous secondary particles that interact with each other. MD simulations were already used to quantify the interparticle forces between spherical silica nanoparticles [14]

* Corresponding author at: Université de Lyon, INSA-Lyon, UCBL, CNRS, MATEIS, 7, Avenue Jean Capelle, Villeurbanne cedex 69621, France.
E-mail address: william.goncalves@tutamail.com (W. Gonçalves).

https://doi.org/10.1016/j.scriptamat.2018.07.039
1359-6462/

to test the applicability of indentation theories based on continuum mechanics [15,16]. However, the MD study of Sun et al. [14] dealt with fully dense silica spherical particles of the order of 2 to 8 nm in diameter and cannot be used to derive the contact force between two highly porous silica secondary particles. To our best knowledge, neither experimental investigations (atomic force microscopy) nor MD simulations have tackled yet this issue. More generally, the indentation behavior of highly nanoporous objects remains poorly known. In particular, size effects that are linked to the interaction of the indenter with nanoligaments have only been tackled very recently [17].

Here, using a combination of MD and Discrete Element Method (DEM) simulations, we investigate the indentation behavior of isolated secondary particles with diameters ranging from 40 to 80 nm with the aim of providing new insights into elementary deformation mechanisms and mechanical properties of these highly nanoporous objects. Also, the indentation laws obtained from the MD simulations described here should enable a multi-scale modeling approach of the granular behavior of aerogel secondary particles based on *e.g.*, DEM simulations, that require interactions forces between particles as input data. Note that we use either the terms indentation or compression for the compression of a nanosphere between two platens as the two problems are self-similar [18].

In this study, we perform MD simulations to investigate the mechanical properties of secondary SiO_2 aerogel nanoparticles under compression using the open-source code LAMMPS [19]. Simulations are carried out using the finite-range approximation of the BKS model for silica [20]. This parameterization is known to reproduce SiO_2 clusters structure and binding energy when compared to Density Functional Theory (DFT) and original BKS as well as structural, surface and mechanical properties of bulk nanoporous silica [12,13].

The sample preparation follows a two-step process as illustrated in Fig. 1. First, a bulk silica nanoporous structure is generated based on the stretching-relaxation method of Kieffer et al. [21] applied to a dense amorphous silica supercell. The resulting density and characteristic porosity size are 250 kg$\cdot$ m^{-3} (equivalent to a 90% porosity structure) and 10 nm, respectively. This density is particularly relevant for comparison with experiments as its pore size distribution [13] matches electron tomography observations [1]. More details on the bulk silica nanoporous structure generation can be found in [13]. Then, finite size nanospheres are carved from the nanoporous structure and further processed *i.e.*, isolated atomic clusters close to the surface are identified and removed using the cluster analysis method of the Ovito software [22]. The structure is then equilibrated during 50 ps at 300 K in the NVT ensemble using the Langevin thermostat and a timestep of 1 fs. See Fig. S1 of the Supplementary Information (SI) for more details about the atomic cluster processing and the relaxation process. Finally, the sample is quenched down to 50 K at 1.25 $\times$ 10^{12} K/s and further equilibrated during 200 ps.

Compression tests are performed using two infinite repulsive force fields with symmetric displacement rates [23-25]. This setup, together with sufficiently slow strain-rates (10^7 s^{-1}) is advantageous to ensure quasi-static conditions especially when modeling highly porous materials (as discussed in section S1 of the SI). Elementary deformation mechanisms are analyzed using the non-affine squared displacement as defined by Falk and Langer (r_{cut} = 10 Å) [26] and the slip vectors analyses. Atomic configurations are visualized using the Ovito software [22].

Fig. 2a shows a compilation of MD indentation curves for the three tested nanosphere sizes *i.e.*, $2R$ = 40, 60 and 80 nm. The three stress-strain curves exhibit comparable behavior with indentation forces that increase non-linearly with increasing strain. However, while the reaction forces on bottom and top platens are approximately equal for $\frac{\delta}{R} \geq 0.06$, they may differ below this range (especially here for the 80 nm nanosphere). The high surface roughness of the nanospheres with dangling ligaments inhibits force equilibrium between the two platens (inset of Fig. 2a). This is actually not specific to the 80 nm sphere. Other simulations carried out on different directions showed a similar non-equilibrated behavior for some other spheres (see Section S3 of the SI).

An unloading sequence was carried out on the 80 nm sphere at $\frac{\delta}{R} = 0.15$. It clearly shows that the indentation of the nanosphere is plastic but with a finite recoverable elastic deformation as illustrated in Fig. 2b (② and ③).

Fig. 2b depict the deformation processes of the 80 nm nanoporous sphere (see Video S1 in the SI for more details). Starting from $\frac{\delta}{R} \geq 0.06$, in addition to the rigid displacement of several ligaments, localized shear zones progressively develop. These plastic events are mainly channeled along the compression axis, which accommodate most of the applied stress due to the spherical geometry of the sample, especially at ligament interconnections. Two types of shearing processes are identified as shown in Fig. 3. The sudden process depicted in Fig. 3a, b (also identified with a black square in Fig. 2b ①) has a very short timescale lower than 100 ps and is associated to a wide and correlated displacement of matter, similar to a crack. Indeed, the displacement vector analysis emphasizes that the

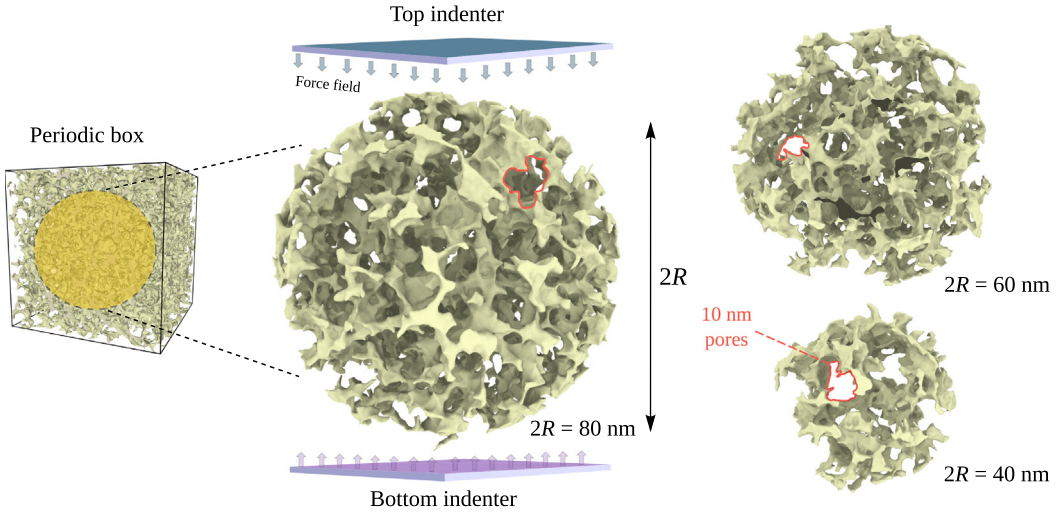

Fig. 1. Surface rendering of silica aerogel secondary particles extracted from a periodic simulation box (250 kg$\cdot$m^{-3} density). The initial sample, with 3.5 million atoms, is generated using the method from Kieffer et al. (see Refs. [13,21] for details).

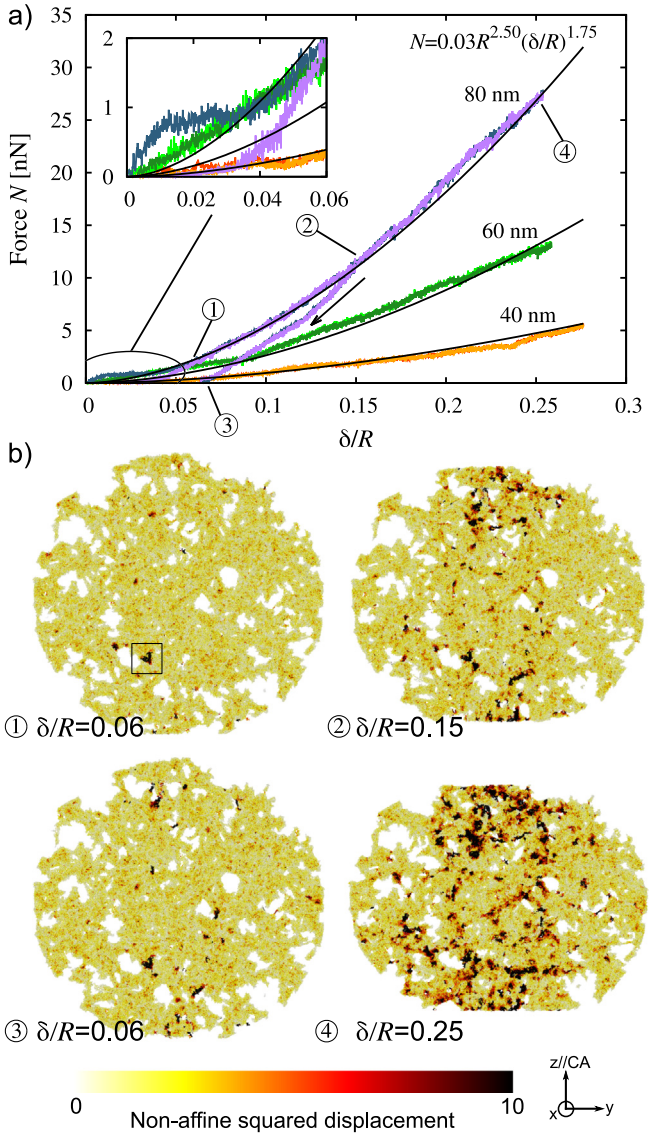

Fig. 2. Mechanical response and deformation processes in 40, 60 and 80 nm silica aerogel nanospheres. a) Evolution of the force of bottom and top platens (strain-rate: $10^7\ s^{-1}$) *vs.* normalized indentation depth $\frac{\delta}{R}$. An unloading sequence is imposed to the 80 nm nanosphere at $\frac{\delta}{R} = 0.15$. The fitted equation (Eq. (2), black lines) provides N (in nN) versus R (in nm). b) Illustration of the plastic deformation processes in the 80 nm nanosphere. The color code refers to the cumulated non-affine squared displacement. b) ① One of the very first shear events at $\frac{\delta}{R} = 0.06$, which is highlighted by a black square and is described more precisely in Fig. 3a, b. ② and ③ Illustrations of the nanosphere before and after the unloading sequence, at $\frac{\delta}{R} = 0.15$ and $\frac{\delta}{R} = 0.06$ respectively. ④ $\frac{\delta}{R} = 0.25$ shows the nanosphere after compression. For the sake of clarity, only a half-part of the nanosphere is shown. The same orientation is used for the four snapshots.

two atomic regions surrounding the shear zone are homogeneously translated along two different directions.

On the other hand, continuously sheared zones with much larger characteristic timescales ($dt \sim 10^5$ ps) are also observed as illustrated in Fig. 3c–e. In most cases, this last process is observed at ligament interconnections, that accommodate shear for a large part of the compression process. See Video S2 and S3 in the SI for more details about both processes. Whatever the nanosphere size, no shear bands were observed. This is attributed to the ligament characteristic diameter (in the range of 3–6 nm), which is smaller than the usual critical length beyond which shear bands start to propagate [27]. Similar elementary deformation processes are observed in the 40 and 60 nm diameter nanoparticles in which dangling ligaments also play a key role, as discussed later.

A natural starting point for analyzing the force-displacement curves in Fig. 2a is the plastic indentation theory, which states that the indentation force scales with R^2 [18]:

$$N = \sigma_0 R^2 \left(\frac{\delta}{R}\right)^{1+\frac{m}{2}} \quad (1)$$

where σ_0 is a material parameter with the unit of stress and m is the strain hardening exponent of the sphere material. Eq. (1) infers that the indentation force scales with R^2 or equivalently that a measure of the stress is size-independent. Fig. 2a shows that this is not the case for the (limited) range of sphere size tested here. Instead, the indentation force (in nN) scales with $R^{2.5}$ (R in nm):

$$N = 0.03 R^{2.5} \left(\frac{\delta}{R}\right)^{1+\frac{m}{2}} \quad (2)$$

A value $m = 1.5$ is obtained from a numerical fit of the three indentation curves shown in Fig. 2a. This is consistent with typical stress-strain curves of highly porous materials that exhibit substantial hardening by densification [28]. This result is also consistent with the MD simulation results of Patil et al. [9] on silica aerogels with 280 kg· m^{-3}, which exhibit similar strain hardening levels up to large compressive strains ($\epsilon \geq 0.7$). Note that the proposed fit only matches satisfactorily the indentation curves for $\frac{\delta}{R} \geq 0.06$ (see inset of Fig. 2a). Below this threshold, the discrete ligaments in contact with the platens dictate the force response.

Surface energy and capillary stress effects play a key role in these nanoporous materials and are responsible for some of their peculiar properties such as their tension-compression asymmetry or their discontinuous plastic Poisson's ratio [29,13]. It would be tempting to ascribe the $R^{2.5}$ size effect obtained in Eq. (2) to surface energy and/or capillary stress effects. To test this, we performed additional fully elastic DEM simulations with particles replacing atoms at the exact same positions (see Section S2 of the SI and [30] for details). Particles are bonded together by elastic beams that transmit tensile, and compressive forces and resisting moments. These simulations do not introduce any surface energy or capillary stress effect in contrast to the MD. Therefore, only the geometry of the sample is probed. DEM simulation results show that in fact the size effect is only due to the internal geometry of the nanosphere (recall that density, $\frac{S}{V}$ ratio and pore size are the same for the three nanospheres). Thus, surface energy and capillary stress effects are not at the origin of the size effect observed here. Instead, as the nanosphere decreases in size, with a given pore size (here approximately 10 nm [13]), the porous structure simply becomes less connected with more dangling ligaments (Section S3 of the SI).

The geometric origin of the size dependence is further confirmed by Fig. 4, which shows the distribution of the cumulate atomic displacements for the three nanosphere sizes in the MD simulations. The displacement is normalized by the nanosphere size and is computed up to $\delta/R = 0.15$. Fig. 4 shows that as the nanosphere size decreases the spread in atomic displacement values increases. This is the signature of a more heterogeneous deformation process as the sample size decreases. In addition, Fig. 4 insets, which show the normalized displacement per atom, clearly emphasize the deviation from the axial symmetry of the deformation originally observed in the 80 nm particle *i.e.*, the deformation of the 40 nm size particle is characterized by the wide and rigid displacement of some ligaments out of the compression axis (shown by the black region at the top right of the 40 nm inset). In other words, in the smaller nanospheres, dangling ligaments

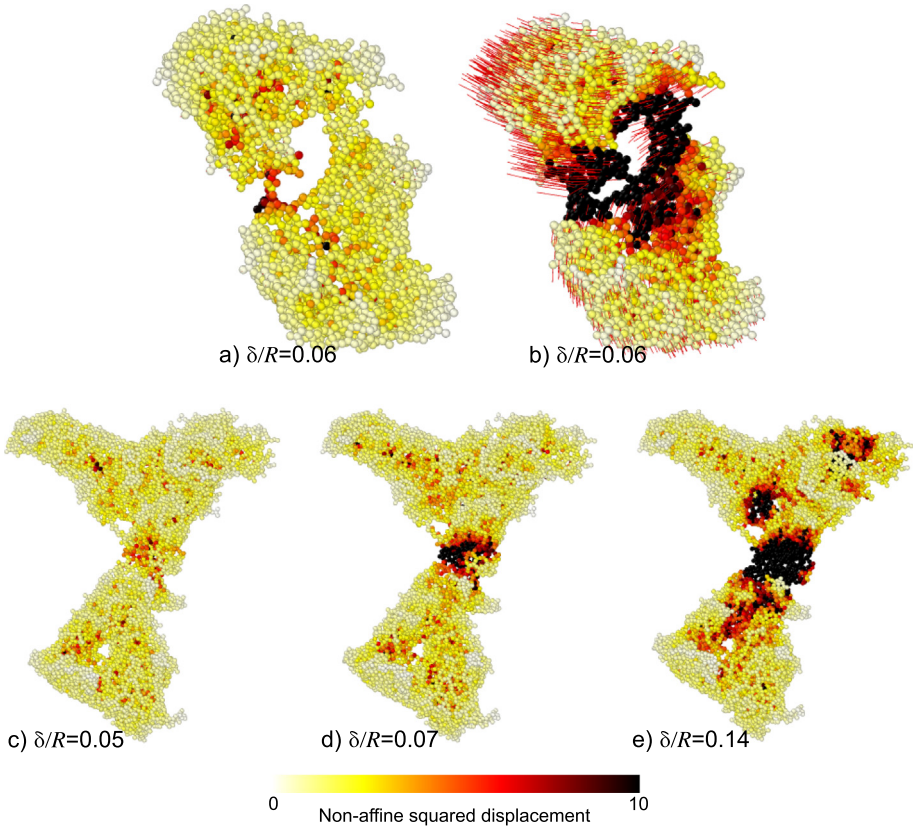

Fig. 3. Sudden and continuous plastic shear events in silica nanoparticles. The two examples shown refer to nanosized subregions, inside the 80 nm nanosphere. Cumulate non-affine squared displacement is used to emphasize sheared zones. a–b) Illustration of a typical sudden shear event with $dt = 100$ ps between the two snapshots. Red arrows refer to instant displacement vectors. This event is located within the black squared region in Fig. 2b. c–e) Example of a continuous plastic event ($dt = 10^4$ ps between the first and last snapshots) where a shear zone grows at the intersection between three silica threads.

experience larger (relative to the size of the nanospheres) and non-axial displacements that are characteristics of rigid body motions. These dangling ligaments do not participate to the stiffness of the nanosphere. They are responsible for the size-dependent response of silica aerogel secondary particles.

In summary, the indentation behavior of highly porous amorphous silica aerogel spheres was investigated using molecular dynamics simulations. For a fixed pore size of the order of 10 nm, typical of secondary aerogel particles, indentation forces are the order of tens of nN. Nanospheres may sustain large strains (strains of the order of 25% were tested here) without fracture. However, the complex structure of the porous spheres with thin ligaments (3 to 6 nm in size), experiences localized shear zones at ligament interconnections. Depending on the size of the nanosphere, ligaments may form a well connected network (80 nm nanosphere) or a poorly one (40 nm nanosphere) with numerous dangling ligaments that do not contribute to the macroscopic stiffness of the nanosphere. As a consequence the indentation force law unveiled by our MD simulations does not scale with the square of the sphere size as in standard indentation theory [18] but with $R^{2.5}$. Here, only one density (250 kg$\cdot$ m^{-3}) has been investigated. Still, for highly porous silica aerogels, dangling ligaments should play a central role in the stress response of the nanosphere. Thus, the departure from the R^2 dependence should hold for a large interval around 250 kg$\cdot$ m^{-3}. It remains to be seen how the power-law exponent evolves with density, but one may expect that it decreases back to two as density increases. We believe that accounting for these original deformation processes at the meso-scale is necessary to better understand the macroscopic response (*e.g.*, in multi-scale modeling approaches) of porous silica aerogels.

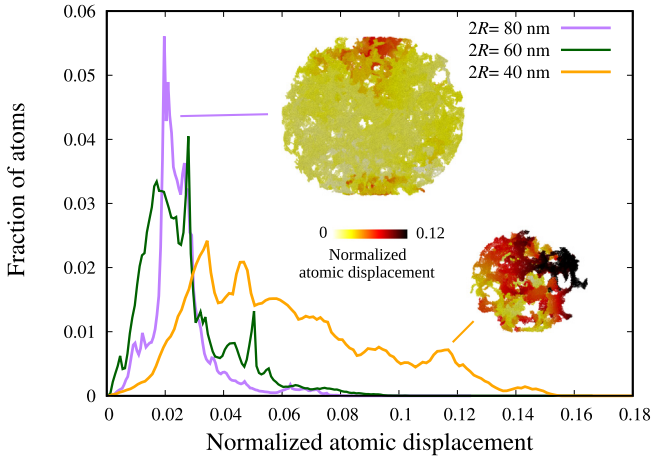

Fig. 4. Distribution of atomic displacements for the three nanosphere sizes, normalized by the nanosphere size. Displacements are calculated for a strain value of $\delta/R = 0.15$ (see Fig. 2).

Supplementary data to this article can be found online at https://doi.org/10.1016/j.scriptamat.2018.07.039.

Acknowledgments

Funding for this project was provided by a grant from la Région Rhône-Alpes (ARC Energies). All the simulations were performed

on the massively parallel computer P2CHPD of FLMSN (Fédération Lyonnaise de Modélisation et Sciences Numériques).

References

[1] L. Roiban, G. Foray, Q. Rong, A. Perret, D. Ihiawakrim, K. Masenelli-Varlot, E. Maire, B. Yrieix, RSC Adv. 6 (2016) 10625–10632.
[2] H. Tamon, T. Sone, M. Okazaki, J. Colloid Interface Sci. 188 (1997) 162–167.
[3] S. Zeng, A. Hunt, W. Cao, R. Greif, J. Heat Transf. 116 (1994) 756–759.
[4] O.-J. Lee, K.-H. Lee, T.J. Yim, S.Y. Kim, K.-P. Yoo, J. Non-Cryst. Solids 298 (2002) 287–292.
[5] M. Koebel, A. Rigacci, P. Achard, J. Sol-Gel Sci. Technol. 63 (2012) 315–339.
[6] T. Woignier, J. Pelous, J. Phalippou, R. Vacher, E. Courtens, J. Non-Cryst. Solids 95 (1987) 1197–1202.
[7] J. Gross, J. Fricke, Nanostruct. Mater. 6 (1995) 905–908.
[8] T. Woignier, J. Reynes, A.H. Alaoui, I. Beurroies, J. Phalippou, J. Non-Cryst. Solids 241 (1998) 45–52.
[9] S.P. Patil, A. Rege, Sagardas, M. Itskov, B. Markert, J. Phys. Chem. B 121 (2017) 5660–5668.
[10] J. Lei, Z. Liu, J. Yeo, T.Y. Ng, Soft Matter 9 (2013) 11367–11373.
[11] J.S.R. Murillo, M.E. Bachlechner, F.A. Campo, E.J. Barbero, J. Non-Cryst. Solids 356 (2010) 1325–1331.
[12] W. Gonçalves, J. Morthomas, P. Chantrenne, M. Perez, G. Foray, C.L. Martin, J. Non-Cryst. Solids 447 (2016) 1–8.
[13] W. Gonçalves, J. Morthomas, P. Chantrenne, M. Perez, G. Foray, C.L. Martin, Acta Mater. 145 (2018) 165–174.
[14] W. Sun, Q. Zeng, A. Yu, K. Kendall, Langmuir 29 (2013) 7825–7837.
[15] B.V. Derjaguin, V.M. Muller, Y.P. Toporov, J. Colloid Interface Sci. 53 (1975) 314–326.
[16] K. Johnson, K. Kendall, A. Roberts, P. R. Soc. A 324 (1971) 301–313.
[17] Y.C. Kim, E.J. Gwak, S. min Ahn, N.R. Kang, H.N. Han, J. il Jang, J.Y. Kim, Scr. Mater. 143 (2018) 10–14.
[18] B. Storåkers, N. Fleck, R. McMeeking, J. Mech. Phys. Solids 47 (1999) 785–815.
[19] S. Plimpton, J. Comput. Phys. 117 (1995) 1–19.
[20] A. Carré, L. Berthier, J. Horbach, S. Ispas, W. Kob, J. Chem. Phys. 127 (2007) 114512.
[21] J. Kieffer, C.A. Angell, J. Non-Cryst. Solids 106 (1988) 336–342.
[22] A. Stukowski, Modell. Simul. Mater. Sci. Eng. 18 (2010) 015012.
[23] I. Issa, J. Amodeo, J. Réthoré, L. Joly-Pottuz, C. Esnouf, J. Morthomas, M. Perez, J. Chevalier, K. Masenelli-Varlot, Acta Mater. 86 (2015) 295–304.
[24] S. Bel Haj Salah, C. Gerard, L. Pizzagalli, Comp. Mater. Sci. 129 (2017) 273–278.
[25] J. Amodeo, K. Lizoul, Mater. Des. 135 (2017) 223–231.
[26] M.L. Falk, J.S. Langer, Phys. Rev. E 57 (1998) 7192–7205.
[27] F. Shimizu, S. Ogata, J. Li, Acta Mater. 54 (2006) 4293–4298.
[28] L.J. Gibson, M.F. Ashby, Cellular Solids: Structure and Properties, Cambridge university press. 1999.
[29] L. Luhrs, B. Zandersons, N. Huber, J. Weissmuller, Nano Lett. 17 (2017) 6258–6266.
[30] R. Kumar, S. Rommel, D. Jauffrès, P. Lhuissier, C.L. Martin, Int. J. Mech. Sci. 110 (2016) 14–21.